Title

Linking preferred orientations to elastic anisotropy in Muderong Shale, AustraliaLinking orientations to anisotropy

Journal

Geophysics, 80(1)

ISSN

0016-8033

Authors

Kanitpanyacharoen, Waruntorn
Vasin, Roman
Wenk, Hans-Rudolf
et al.

Publication Date

2015

DOI

10.1190/geo2014-0236.1

Peer reviewed

GEOPHYSICS, VOL. 80, NO. 1 (JANUARY-FEBRUARY 2015); P. C9–C19, 6 FIGS., 3 TABLES.
10.1190/GEO2014-0236.1

Linking preferred orientations to elastic anisotropy in Muderong Shale, Australia

Waruntorn Kanitpanyacharoen[1], Roman Vasin[2], Hans-Rudolf Wenk[3], and David. N. Dewhurst[4]

ABSTRACT

The significance of shales for unconventional hydrocarbon reservoirs, nuclear waste repositories, and geologic carbon storage has opened new research frontiers in geophysics. Among many of its unique physical properties, elastic anisotropy had long been investigated by experimental and computational approaches. Here, we calculated elastic properties of Cretaceous Muderong Shale from Australia with a self-consistent averaging method based on microstructural information. The volume fraction and crystallographic preferred orientation distributions of constituent minerals were based on synchrotron x-ray diffraction experiments. Aspect ratios of minerals and pores, determined from scanning electron microscopy, were introduced in the self-consistent averaging. Our analysis suggested that phyllosilicates (i.e., illite-mica, illite-smectite, kaolinite, and chlorite) were dominant with ~70 vol.%. The shape of clay platelets displayed an average aspect ratio of 0.05. These platelets were aligned parallel to the bedding plane with a high degree of preferred orientation. The estimated porosity at ambient pressure was ~17 vol.% and was divided into equiaxial pores and flat pores with an average aspect ratio of 0.01. Our model gave results that compared satisfactorily with values derived from ultrasonic velocity measurements, confirming the validity and reliability of our approximations and averaging approach.

INTRODUCTION

Shale is a phyllosilicate-rich and inherently heterogeneous rock, which traditionally has been recognized as a cap rock in hydrocarbon reservoirs (Tissot and Welte, 1984; Aplin and Larter, 2005). With the advancement of technology, natural gas can be produced directly from shale reservoirs. Shale is also considered as a seal rock for nuclear waste repositories (Mallants et al., 2001; Bossart and Thury, 2007) and geologic carbon storage due to its low permeability and adsorption capability (Kennedy et al., 2002; Xu et al., 2005; Tao and Clarens, 2013). However, many shale physical and chemical fundamentals are still poorly understood. In this context, there has been great interest in elastic anisotropy, which plays a crucial role in identifying subsurface lithologies.

The elastic anisotropy of shale is attributed to the combined effect of clay preferred orientation (e.g., Hornby et al., 1994; Sayers, 1994) as well as pore, crack, and kerogen alignment at various scales (e.g., Nur and Simmons, 1969; Vernik and Nur, 1992). Clay platelets preferentially align parallel to the bedding plane during sedimentation, compaction, and burial diagenesis, allowing seismic waves to propagate faster in this direction (e.g., Kaarsberg, 1959; Aplin et al., 2006). P-wave velocity and x-ray diffraction (XRD) measurements both indicate that shales are largely transversely isotropic for all stages of compaction (Kaarsberg, 1959; Sayers, 1994). In addition, flat pores and cracks also tend to align subparallel to the bedding plane and amplify the elastic anisotropy of shale (e.g., Jones and Wang, 1981; Sayers, 2008; Keller et al., 2011). Several studies have characterized pore types and pore shapes from micro- to nano-scale (e.g., Loucks et al., 2009, 2012; Kanitpanyacharoen et al., 2011; Keller et al., 2011, 2013; Kuila and Prasad, 2013) to describe their influence on elastic properties.

Manuscript received by the Editor 19 May 2014; revised manuscript received 21 August 2014; published online 30 December 2014.
[1]University of California, Department of Earth and Planetary Science, Berkeley, California, USA and Chulalongkorn University, Department of Geology, Faculty of Science, Bangkok, Thailand. E-mail: waruntorn.k@chula.ac.th.
[2]University of California, Department of Earth and Planetary Science, Berkeley, California, USA and Joint Institute for Nuclear Research, Frank Laboratory of Neutron Physics, Dubna, Russia. E-mail: olddragon@mail.ru.
[3]University of California, Department of Earth and Planetary Science, Berkeley, California, USA. E-mail: wenk@berkeley.edu.
[4]CSIRO Energy, Perth, Australia. E-mail: david.dewhurst@csiro.au.

Direct laboratory measurements of elastic wave propagation in different directions have been used to explore the importance of shale composition and to quantify trends of elastic anisotropy upon compaction (e.g., Johnston, 1987; Vernik and Nur, 1992; Hornby, 1998; Pham et al., 2002; Wang, 2002; Dewhurst and Siggins, 2006; Voltolini et al., 2009; Nadri et al., 2012). Several modeling approaches, assuming shale as a transverse isotropic body, have been proposed to explain anisotropic elastic properties, including self-consistent theories and hypothetical assumptions of microstructures and preferred orientation (e.g., Rundle and Schuler, 1981; Hornby et al., 1994; Jakobsen et al., 2000; Dræge et al., 2006; Ortega et al., 2007; Moyano et al., 2012). Although providing qualitatively convincing results, most of these modeling approaches have not fully taken clay preferred orientations, elastic anisotropy of minerals, and microstructural information into account. Applying a recently proposed self-consistent approach that relies on measured microstructural data (Matthies, 2010, 2012), a study by Vasin et al. (2013) was able to explain experimentally determined elastic properties of Kimmeridge Shale (Hornby, 1998) within error margins. Here, we are applying the same method to a different sample, Cretaceous Muderong Shale from Australia, for which ultrasonic velocity data are available (Dewhurst and Siggins, 2006).

The approach we use requires the knowledge of mineral elastic properties, volume fractions, crystallographic orientation distributions, and porosity. The shapes of mineral grains and pores as well as their shape orientation distributions also have to be quantified. Preferred orientations of component minerals and volume fractions are determined from synchrotron XRD data, whereas shapes of grains as well as pores are estimated from scanning electron microscopy (SEM) observations.

MUDERONG SHALE SAMPLE

Origin and general description

The Muderong Shale from the Carnarvon Basin on the Northwest Shelf of Australia has been extensively studied due to its sealing capacity for the largest hydrocarbon producing region in Australia (e.g., Dewhurst et al., 2002; Dewhurst and Hennig, 2003). Most of hydrocarbon resources in the Carnarvon Basin are trapped beneath the Muderong Shale. A study by Cockbain (1989) reports that the Muderong Shale was deposited when the Barrow Group delta system became inactive during the Neocomian transgression. This sealing unit is laterally extensive, occurring between depths of 500–3500 m, with thickness variations from 5 m to more than 800 m. At these depths, the shale has undergone mechanical compaction and diagenesis, decreasing pore size and strengthening the preferred orientation of phyllosilicates. The same sample of Muderong Shale described by Dewhurst and Siggins (2006) was used in this study. This sample was cored from the offshore northern Carnarvon Basin at a depth of about 1120 m.

Overall, the sample is clay-rich (i.e., illite, illite-smectite mixed layer, kaolinite, and chlorite), extremely fine-grained, and nonlaminated. A low cation exchange capacity around 20 meq/100 g is reported in Dewhurst et al. (2002). At ambient conditions, the porosity is about 17 vol.%, as determined by mercury injection capillary pressure (Dewhurst et al., 2002). Permeability is less than 1 nD, and the measured bulk density is 2.33 g/cm^3. The sample contains a very small portion of kerogen, with a total organic content less than 1 vol.%. Further information about geomechanical properties and sealing capacity of the Muderong Shale is provided in Dewhurst et al. (2002) and Dewhurst and Hennig (2003).

Elastic properties

Dewhurst and Siggins (2006) determine five independent components of a stiffness tensor of the transversely isotropic Muderong Shale at different pressures from ultrasonic measurements. In a standard two-index Voigt notation, these elastic coefficients are $C_{11} = C_{22}$, $C_{12} = C_{11} - 2C_{66}$, $C_{13} = C_{23}$, C_{33}, and $C_{44} = C_{55}$; all others are equal to zero.

Measurement of ultrasonic velocities was achieved through the triaxial testing apparatus, which is capable of reaching up to 70 MPa confining and pore pressure and up to 400 MPa axial stress on a 1.5″ diameter cylindrical sample. P- and S-wave transducers were located in the platens to allow axial measurement of ultrasonic velocities in core plugs. Similarly, P- and S-wave transducers were mounted around the center of the Viton membrane to allow measurements across the core diameter. Finally, P-wave transducers were located at 45° across the membrane. This configuration allows an estimate of the full elastic tensor to be made for a transversely isotropic material. More complete details of the ultrasonic testing procedures are described in Dewhurst and Siggins (2006).

Consolidated undrained multiple stage triaxial test (Fjær et al., 2008) were run on the Muderong Shale, with initial confining and pore pressures of 10 and 5 MPa, respectively. Pore pressure lines were closed during application of differential stress, resulting in undrained loading. Differential stress was increased until close to failure at a given confining pressure at which point the axial load was decreased to ~0.5 kN and pore pressure was drained to back pressure. Once the pore pressures were stabilized, confining pressure was increased to the next level and pore pressures again was allowed to equilibrate before a new application of axial load. The axial load was applied in the direction parallel to the bedding plane. Ultrasonic readings were taken at the pore pressure equilibration point and during the undrained axial loading step.

One issue with this experimental technique is to determine whether wave arrivals are group or phase velocities (e.g., Dellinger and Vernik, 1994; Hornby, 1998) because the latter are required to properly calculate the full elastic tensor from the Christoffel equations. Although the waves traveling axially and radially through the core plug are traveling along principal axes and thus are phase velocities, modeling results from Dewhurst and Siggins (2006) indicate that the P-waves traveling at 45° to the sample axis (and thus to the bedding plane) were group velocities. Calculation of C_{13} requires a phase velocity value. Dewhurst and Siggins (2006) solve simultaneously for the eigenvalues of the Christoffel equations (e.g., Helbig and Schoenberg, 1987; Tsvankin, 2001) for a transversely isotropic material, giving θ (the angle between the normal to the wavefront and the transducer), the phase velocity value and ultimately C_{13}, at each stress condition. Recorded waveforms are shown in Dewhurst and Siggins (2006), and these authors estimated velocity errors of ~0.5% due to uncertainty of picking arrival times. This translated to errors in elastic constants of less than 1%, except for C_{13}, which was closer to 2%. Errors in P- and S-wave anisotropy were also ~2%, but that for Thomsen's δ value was ~13%. It should also be noted that there are significant further uncertainties in calculating C_{13} and δ as a result of using a single off-axis raypath. New techniques using multiple raypaths have been developed since the Dewhurst and Siggins (2006) paper, which show that having a

redundancy of 65–70 raypaths puts far better constraints and lower error values on laboratory determinations of δ (Nadri et al., 2012; Sarout et al., 2014).

EXPERIMENTAL DETERMINATION OF THE SHALE MICROSTRUCTURE

Scanning electron microscopy

A polished slice of the Muderong Shale was carbon coated and examined with a Zeiss Evo MA10 low-vacuum SEM equipped with an EDAX energy-dispersive spectroscopy system at the University of California, Berkeley. The SEM was operated with an accelerating voltage of 20 kV and a probe current of 20 nA to collect images. The shale was analyzed for mineralogic composition and microstructure. The brightness variation of the backscattered (BE) SEM images, ranging from low (black) to high (white), is mainly due to the contrast in atomic number, with high atomic numbers appearing brighter. A BE-SEM image shows complex microstructures of authigenic illite-smectite, detrital illite-mica, and kaolinite platelets, and some coarse-grained quartz, feldspars, and pyrite (Figure 1).

BE-SEM images illustrate the heterogeneous microstructure of Muderong Shale with a horizontal bedding plane. Fine-grained phyllosilicate minerals (dark gray) dominate the microstructure with the ubiquitous presence of different pore types (black) (Figure 1a). Coarse-grained quartz fragments are also observed and often associated with small pores around the grain boundary. Figure 1b displays a relatively large and elongated detrital illite-mica grain with a parallel thin pore. Some low-aspect-ratio cracks are likely due to stress relief or desiccation. Smaller pores are also observed in Figure 1b. Figure 1c and 1d shows spherical pores (black) and pyrite (white), which are randomly distributed in the sample.

Mineral and pore aspect ratios are estimated from SEM images and used as input parameters in the self-consistent routines for calculating bulk elastic properties, assuming ellipsoidal inclusion shape. The ellipsoidal shape here is expressed by three numbers $\{x:y:z\}$, representing the relation between the shortest axis (z) and two axes of equal length (x and y). In general, the shape of phyllosilicates average to the platelet (oblate spheroid) with $\{x:y:z\}$ axis ratios of $\{1:1:0.05\}$ (i.e., the aspect ratio of these grains is 0.05). Quartz grains are more or less equiaxial and are considered as spheres ($\{1:1:1\}$ axis ratio). There are spherical as well as platelet-shaped pores with average axis ratios $\{1:1:0.01\}$ (aspect ratio of 0.01).

Synchrotron x-ray diffraction

A small piece of the Muderong Shale was cut perpendicular to the bedding plane into a thin disk (2 mm thick and 2 cm in diameter) and embedded in epoxy. The epoxy disk was polished until the shale surface was exposed. To prevent clays from swelling, kerosene was used for cutting and polishing. Synchrotron XRD experiments were conducted at the 11-ID-C high-energy beamline of the Advanced Photon Source of the Argonne National Laboratory. A monochromatic x-ray beam with a wavelength of 0.10789 Å (energy of 115 keV) was collimated to 1×1 mm. The sample was analyzed in transmission. During x-ray exposure, the sample was translated over 5 mm along the horizontal axis (and perpendicular to the bedding plane) to obtain a representative sample volume average (~10 mm^3) and good grain statistics. Diffraction patterns were recorded with a PerkinElmer amorphous silicon detector (2048×2048 pixels) situated about 2 m away from the sample. A typical diffraction image is shown in Figure 2a. Seven images were recorded by rotating the sample around the horizontal axis, from −45° to 45° in 15° increments, to provide sufficient orientation coverage for texture analysis. Each image was integrated over 10° azimuthal sectors to obtain a total of 36 diffraction patterns, representing distinctively oriented lattice planes. A stack of all 36 patterns resulting from one image is shown in Figure 2b.

The XRD patterns ($36 \times 7 = 252$) were then analyzed by the Rietveld method (Rietveld, 1969) implemented in materials analysis using diffraction (MAUD) software (Lutterotti et al., 1997, 2010; Wenk et al., 2014), which relies on a least-squares fit to minimize the difference between experimental diffraction data and a calculated model. A polynomial function with five coefficients was used to refine the background of each image, and five minerals were considered, with corresponding crystallographic information from the literature: kaolinite (Bish and Von Dreele, 1989), illite-muscovite (Gualtieri, 2000), illite-smectite modeled after phengite (Plançon et al., 1985), quartz (Antao et al., 2008), and chlorite (Joswig et al., 1980). Other minor phases, e.g., orthoclase and pyrite with contributions less than 1 vol.%, were neglected from the analysis. The stacking-disordered structure of illite-smectite was modeled with the approach described by Ufer et al. (2004) included in MAUD (Lutterotti et al., 2010). Note that for the texture analysis methods, the first setting for monoclinic

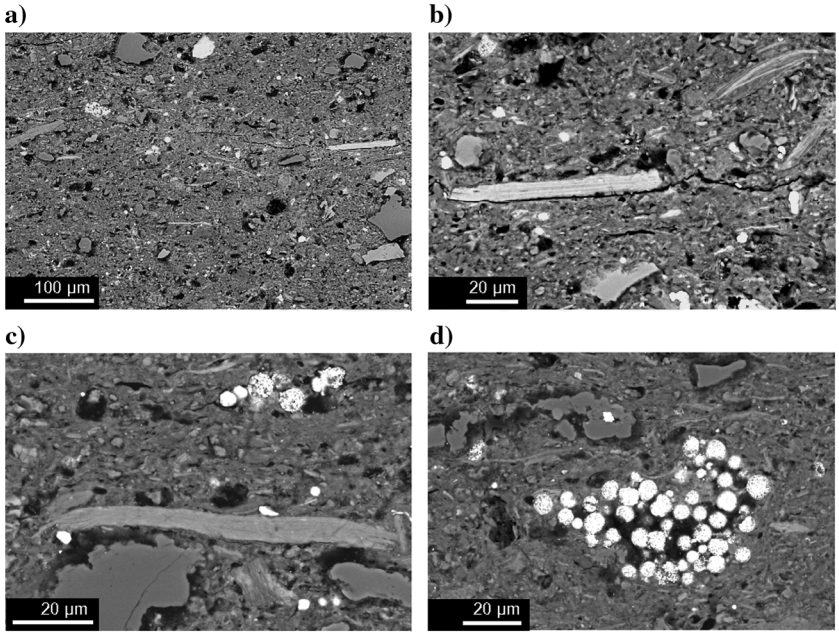

Figure 1. BE-SEM images of Muderong Shale. (a) General overview displaying a phyllosilicate matrix with inclusions of platy detrital mica and angular quartz. (b) Detail of illite-muscovite platelet and flat and equiaxial pores and cracks. (c) Fe and Mg containing mica (elongate, dark gray) and some spherical pyrite. (d) Framboidal pyrite aggregate in clay matrix.

crystals such as illite-mica and illite-smectite needs to be applied; i.e., (100) is the cleavage plane instead of a more familiar second setting with (001) as the cleavage plane (Matthies and Wenk, 2009). This was also taken into account in the calculations of physical properties of the polycrystalline shale (all the elastic tensors of monoclinic crystals have been transformed into first monoclinic setting). Except for labels of lattice planes *hkl* in text, tables, and figures, we use the more conventional second setting.

A comparison of the calculated model with experimental spectra (Figure 2 top and bottom) indicates a close similarity, indicative of an excellent fit, in intensities as well as the position of diffraction peaks. Quantitative results from Rietveld refinement include crystallographic preferred orientation distribution functions (ODFs) and volume fractions of phyllosilicates (Table 1).

We assumed a random orientation distribution for quartz that does not show significant intensity variations along Debye rings (Figure 2b). For phyllosilicates, preferred orientation distributions (or texture) were computed by the EWIMV algorithm (Matthies and Vinel, 1982; Lutterotti et al., 2010), using 10° resolution for the ODFs, without imposing axial symmetry around the bedding plane normal. The ODFs were exported from MAUD and smoothed with a 7.5° Gaussian filter in the BEARTEX software (Wenk et al., 1998) to calculate pole figures (Figure 3). The pole figures show more or less axial symmetry around the pole to the bedding plane. This transverse isotropy is common to most shales, and deviations from

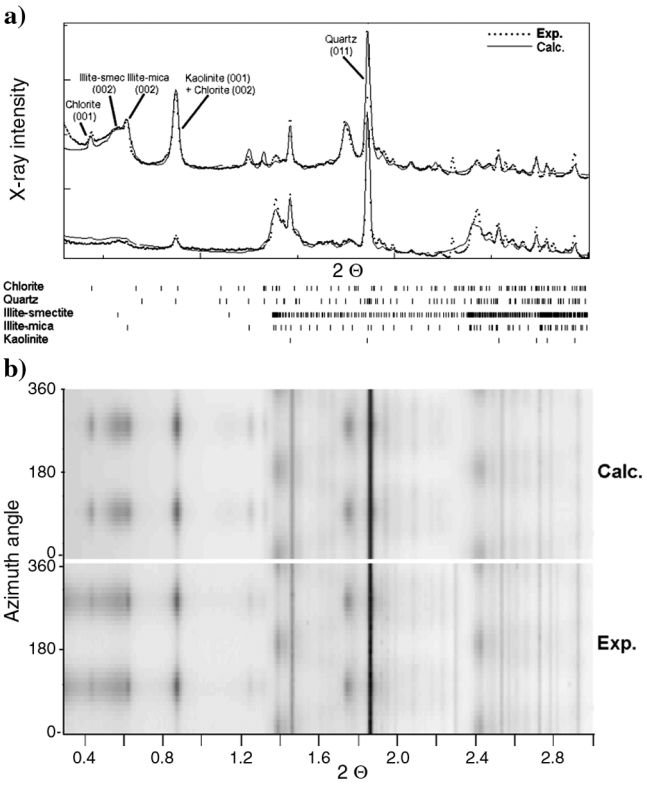

Figure 2. (a) XRD pattern of Muderong Shale. Some diffraction peaks are indexed. A thick solid line shows experimental data, and a thin dashed line indicates the Rietveld fit. Locations of diffraction peaks for individual phases are indicated at bottom. (b) A stack of diffraction patterns displays preferred orientation of phyllosilicates and compares the model (top) with the experimental data (bottom).

it can be explained by the incomplete pole figure coverage (Wenk et al., 2014). Thus, we enforce the axial symmetry of preferred orientations by averaging orientation distributions around the bedding plane normal. Textures can then be described by a simple pole density profile from parallel to perpendicular to the bedding plane normal (Figure 4). These textures will be used for the elastic property calculations.

The mineralogy of Muderong Shale is dominated by clay minerals, which comprise more than 70 vol.%, with significant quartz content of 28.3 vol.% (Table 1). Illite, including illite-mica and mixed layered illite-smectite, is the most abundant phyllosilicate, with a total of 52 vol.%. Kaolinite and chlorite are also present with a relatively minor amounts of 14.4 vol.% and 4.1 vol.%, respectively. Illite-mica and chlorite show the highest degrees of preferred orientation, and illite-smectite, probably authigenic, exhibits relatively weaker degrees of preferred orientation (Figures 3 and 4), which is consistent with previous studies on shales (e.g., Wenk et al., 2008, 2010; Kanitpanyacharoen et al., 2011, 2012).

MODELS OF ELASTIC PROPERTIES

We model elastic properties of shale using anisotropic elastic properties of minerals and considering volume fractions, preferred orientations and shape of mineral grains and pores (aspect ratios). We start at an increased pressure (more than 50 MPa) in which some of the pores, especially those that are "empty" or air-filled, are closed and investigate if it is possible to describe elastic properties at lower pressures by increasing the porosity of the model.

For kaolinite, illite-mica, and illite-smectite, there are no reliable experimentally determined elastic properties and there is considerable uncertainty about results from ab initio calculations (Militzer et al., 2011). For quartz, we use those measured by Heyliger et al. (2003). Since the elastic properties of chlorite are unknown, we use a set of elastic coefficients for "hexagonal" biotite determined by Aleksandrov and Ryzhova (1961). This should not introduce a significant error due to low volume fraction of chlorite in the shale (Table 1). All the single crystal elastic stiffness coefficients are listed in Table 2, as well as the mineral densities. Uncertainties about single crystal elastic constants of phyllosilicates are a significant limitation of the model.

Vasin et al. (2013) note that due to the relationship of the crystal structure of monoclinic and triclinic phyllosilicates and the morphology of their grains (i.e., (001) is the platelet plane), it is possible to calculate their shape ODFs from measured crystal ODFs. In

Table 1. Volume fractions, minimum, and maximum values on pole figure (001) for the major minerals comprising the Muderong Shale sample.

Mineral	Volume fraction	Pole figure (001) minimum (m.r.d.)	Pole figure (001) maximum (m.r.d.)
Quartz	0.283	—	—
Kaolinite	0.144	0.24	3.99
Illite-smectite	0.323	0.45	3.58
Illite-mica	0.209	0.17	5.52
Chlorite	0.041	0.21	4.69

general, three different coordinate systems are necessary to describe orientation relationships in a polycrystalline material with non-spherical grains. The crystal coordinate system K_B is fixed to the crystal unit cell according to a set of specific rules (Matthies et al., 1988); the grain coordinate system K_E is fixed onto the oblate spheroidal — or platelet-shaped — grain (axes of K_E are parallel to axes of the ellipsoid, approximating the grain shape); and the macroscopic coordinate system K_A is fixed onto the sample (in our case of the transversely isotropic shale sample, axis Z_A is normal to the bedding). Shape ODF relates K_E to K_A in the same manner that the crystal ODF relates K_B to K_A. In phyllosilicates, K_E is usually tilted with respect to K_B. For triclinic kaolinite, the platelet-shaped grain is parallel to the (001) plane, and Z_E is normal to it, whereas Z_B is fixed to the (001) direction and thus is not parallel to Z_E. By considering this additional tilt of K_E to K_B, it is possible to construct the shape ODFs. Also, to perform ODF-averaging operations, elastic tensors of phyllosilicates have to be transformed into K_E, except for chlorite with idealized hexagonal symmetry.

Modeling of materials with complex microstructures such as shales is a difficult and cumbersome task. Using Kimmeridge Shale as an example, Vasin et al. (2013) show that by making some simplifying assumptions (e.g., substituting actual shape distributions of phyllosilicate grains with the single oblate spheroidal grain shape, etc.), it is possible to reach model elastic coefficients closely corresponding to those derived experimentally with ultrasonic methods (Hornby, 1998). Two models have been proposed, a self-consistent model and a differential effective medium (DEM) model. Both include oblate spheroidal phyllosilicate grain shapes with the axis ratio $\{1:1:0.05\}$ (in K_E) and a spherical grain shape for other minerals (e.g., quartz), and both models feature two types of water-filled pores: spherical $\{1:1:1\}$ and low-aspect-ratio pores with the axis ratio $\{1:1:0.01\}$. Here, we use the same grain and pore shapes. Only a brief summary of modeling steps is described here, and for complete procedures we refer to Vasin et al. (2013).

Self-consistent GeoMIXSelf model

The first model uses only a well-established self-consistent method (e.g., Kröner, 1958; Budiansky, 1965; Hill, 1965; Morris, 1970) based on Eshelby's (1957) inclusion principle. We use the same GeoMIXself (GMS) algorithm (Matthies, 2010, 2012) as Vasin et al. (2013). It is a modification of a self-consistent method using the elements of the geometric mean averaging to satisfy the inversion relation for the model bulk elastic tensor. The calculated stiffness of the polycrystalline medium is exactly equal to the inverse compliance. In this model, first, elastic properties of the "crystalline" part, which contains only mineral orientation distributions, volume fractions, and aspect ratio information of the grains, are calculated. Corresponding values of bulk stiffness tensor components for the Muderong Shale are given in Table 3, no. 1.

At the next modeling step, low-aspect-ratio $\{1:1:0.01\}$ and spherical pores $\{1:1:1\}$ are added into the crystalline part. Dewhurst and Siggins (2006) report the porosity of the Muderong Shale to be ~17 vol.% at atmospheric pressure. At increased net pressure (or vertical effective stress) of more than 50 MPa, some pores, especially "air-filled" pores, should be closed. The reduction of porosity by 2 vol.% could be contributed by a combination of pore closure and experimental errors. Thus, it is safe to assume a porosity value of ≈15 vol.% for Muderong Shale at 50 MPa net pressure. The model of Kimmeridge Shale developed by Vasin et al. (2013) was simplified by substituting the real distribution of pore shapes with two types of pores: 3 vol.% of spherical and 3.5 vol.% of low-aspect-ratio water-filled pores (with bulk modulus of 2.2 GPa and shear modulus equal to zero, Hornby et al., 1994; Arns et al., 2002). We assume that the ratio of low-aspect-ratio and spherical pores volumes of about 1 : 1 could be preserved in the case of Muderong Shale, which results in 7.5 vol.% of spherical and 7.5 vol.% of low-aspect-ratio water-filled pores in the sample.

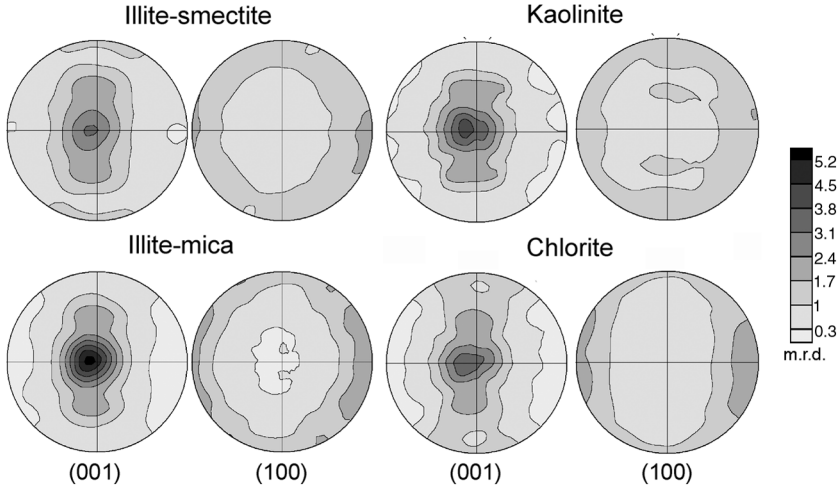

Figure 3. Pole figures of kaolinite, illite-mica, illite-smectite, and chlorite. Equal area projections on the bedding plane, linear pole density scale, values are in multiples of random distribution (m.r.d.). For texture strength, see also Table 1.

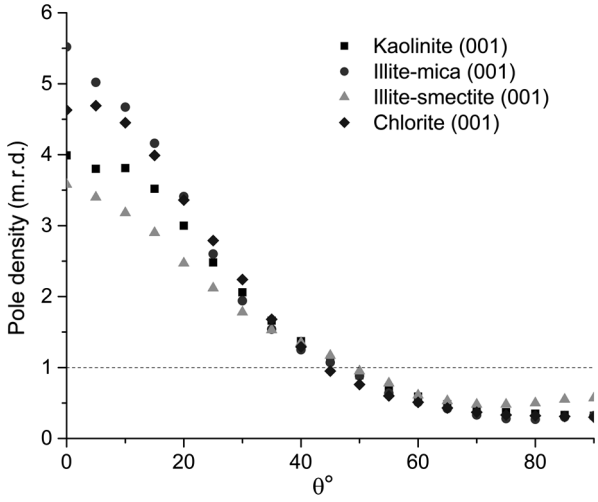

Figure 4. (001) Pole figure profiles as function of the angle to the bedding plane.

For low-aspect-ratio pores, we construct a model axially symmetrical orientation distribution, which is similar to those of phyllosilicates and consists of random and Gaussian fiber components. A volume of a random component and a width of the Gaussian component is to some degree constrained by characteristics of phyllosilicate textures. About 20 vol.% of phyllosilicates are randomly oriented (Table 1), constituting the "random component" in our model (0.2 m.r.d.). Vasin et al. (2013) show that a satisfactory width of a Gaussian component is 35°; this is 10°–15° lower than the mean width of the fiber components of phyllosilicate textures (Figure 5).

Table 2. Single crystal elastic constants of minerals composing the Muderong Shale sample in standard two-index Voigt notation C_{ij} (GPa) and their density values ρ (g/cm^3). Values are given for crystal coordinate system K_B and shape coordinate system K_E. For monoclinic illite, the first setting is used (see also Vasin et al., 2013).

Mineral	Kaolinite		Illite-mica		Illite-smectite		Quartz	Chlorite
ρ	2.599		2.844		2.8247		2.6466	2.950
Reference	Militzer et al. (2011)		Militzer et al. (2011)		Militzer et al. (2011)		Heyliger et al. (2003)	Aleksandrov and Ryzhova (1961)
Coordinate system	K_B	K_E	K_B	K_E	K_B	K_E	$K_B = K_E$	$K_B = K_E$
C_{11}	169.1	187.42	60.3	60.14	27.2	25.15	87.26	186.00
C_{12}	66.1	70.41	27.2	25.55	13.2	5.89	6.57	32.40
C_{13}	15.4	4.84	23.5	23.97	5.2	2.43	11.95	11.60
C_{14}	−0.4	−2.24	0	0	0	0	−17.18	0
C_{15}	−34.0	1.24	0	0	0	0	0	0
C_{16}	−7.8	−7.51	−1.0	0.03	−5.4	0.60	0	0
C_{22}	179.7	179.70	180.9	184.36	153.9	170.58	87.26	186.00
C_{23}	10.2	5.89	53.4	52.93	25.1	27.87	11.95	11.60
C_{24}	−3.4	−3.31	0	0	0	0	17.18	0
C_{25}	−16.1	0.03	0	0	0	0	0	0
C_{26}	−0.1	0.78	−14.7	−5.02	−30.3	0.16	0	0
C_{33}	81.1	83.91	170.0	170.00	188.5	188.50	105.80	54.00
C_{34}	−2.9	−2.99	0	0	0	0	0	0
C_{35}	6.7	−2.88	0	0	0	0	0	0
C_{36}	−0.1	0.73	1.4	3.97	−8.2	−2.13	0	0
C_{44}	17.0	13.52	70.5	70.42	55.4	60.34	57.15	5.80
C_{45}	−0.7	−0.23	−1.8	2.75	−15.9	−2.52	0	0
C_{46}	−12.4	−0.59	0	0	0	0	0	0
C_{55}	26.6	16.04	18.4	18.48	10.4	5.46	57.15	5.80
C_{56}	1.1	−0.94	0	0	0	0	−17.18	0
C_{66}	57.6	61.08	23.8	22.15	24.8	17.49	40.35	76.80

Table 3. Comparing elastic coefficients (in GPa) of different models (no. 1–2, 4–5, and 7) of the Muderong Shale with experimental results at high and low stress (no. 3 and 6).

No.	C_{11}	C_{13}	C_{33}	C_{44}	C_{66}	Remarks
1	93.1	19.1	65.7	27.6	35.8	Without pores
2	26.3	12.5	18.2	2.8	6.8	GMS model, 15 vol.% porosity
3	26.6	16.2	18.3	4.5	8.8	Measured at 52.5 MPa (Dewhurst and Siggins, 2006)
4	17.8	8.0	11.4	1.9	4.6	GMS model, 15.8 vol.% porosity, including 0.1 vol.% of empty pores
5	19.3	8.4	12.2	2.1	5.2	GMS model, 15.5 vol.% porosity, including 0.1 vol.% of empty pores
6	19.5	7.6	13.2	3.0	6.4	Measured at 5 MPa (Dewhurst and Siggins, 2006)
7	28.0	12.5	14.3	2.6	7.2	DEM model, 27.2 vol.% porosity

It is probably due to a higher volume fraction of pores that tend to orient practically parallel to the bedding plane. These pores could be considered as "meso" or "macroscopic" because they are related to the bedding plane, which is a feature of the material itself, rather than "micropores" that are related (and are mostly parallel) to platelet-shaped phyllosilicate grains. Thus, we use a fiber texture for low-aspect-ratio pores with 0.2 of random component and 0.8 of Gaussian component with a full width at half-maximum of 35°.

We add 7.5 vol.% of spherical water-filled pores and 7.5 vol.% of {1:1:0.01} water-filled pores with a fiber texture into the crystalline part of the shale, using the GMS algorithm. Resulting elastic coefficients decrease significantly (Table 3, no. 2) and are very close to those estimated by Dewhurst and Siggins (2006) (Table 3, no. 3), with the biggest difference in C_{13}; its model value is lower by ≈3.7 GPa.

Vasin et al. (2013) show that elastic coefficients of the shale at lower pressure values could be calculated by increasing a content of low-aspect-ratio pores to the high-pressure model and also adding a very small volume fraction of air-filled pores (with all elastic coefficients equal to zero). They were able to reach a satisfactory agreement between measured and model elastic properties for Kimmeridge Shale at 5 MPa pressure by adding 0.7 vol.% of water-filled and 0.1 vol.% of air-filled low-aspect-ratio pores into the model shale at 80 MPa pressure.

In the case of Muderong Shale, additional 0.7 vol.% of water-filled and 0.1 vol.% of air-filled low-aspect-ratio pores in model no. 2 in Table 3 lead to elastic coefficients of model no. 4 (Table 3) that are all slightly lower than those given by Dewhurst and Siggins (2006) (no. 6 in Table 3). If only 0.4 vol.% of water-filled pores is added instead of 0.7 vol.%, a model of Muderong Shale with 7.5 vol.% of spherical water-filled pores, 7.9 vol.% of water-filled pores, and 0.1 vol.% of air-filled pores with {1:1:0.01} aspect ratio and fiber texture has higher elastic coefficients listed in Table 3, no. 5. They are in better agreement with the experiment, and the total porosity value in this case is 15.5 vol.%, which is also reasonably close to the estimated value at atmospheric pressure of ~17 vol.% (Dewhurst and Siggins, 2006).

Model using the differential effective medium approach

We also used the DEM model introduced by Bruggeman (1935) and applied by Hornby et al. (1994) for shales. In this model, first, properties of effective "units" composed of phyllosilicate grains and low-aspect-ratio water-filled pores are calculated using a stepwise procedure. At the first step of this scheme, 50 vol.% of mineral grains and 50 vol.% of water-filled pores with their corresponding shapes are mixed with the self-consistent GMS algorithm. Phyllosilicate platelets and low-aspect-ratio pores are considered to be fully aligned to each other. Afterward, at each step, infinitesimal volumes of mineral grains are added as inclusions into the host material, which is the homogeneous effective medium obtained at the previous step, with the same self-consistent algorithm, until the volume fraction of low-aspect-ratio pores is decreased to the expected value. The same procedure with the same parameters is performed for each of the phyllosilicates. Then, the geometric mean (Matthies and Humbert, 1995) method is applied to average elastic properties of these mineral-water "units." Finally, a small amount (about 1 vol.%) of water-filled spherical pores is added into the model (Vasin et al., 2013).

We applied this modeling procedure to Muderong Shale, and one set of the model elastic coefficients is given as model no. 7 (Table 3). They are reasonably close to the GMS model (no. 2, Table 3) and experimental values (no. 3, Table 3). But the total porosity of this model is ≈27.2 vol.%, including 2 vol.% of spherical pores and 25.2 vol.% of low-aspect-ratio pores, which is far above the experimentally estimated porosity of ~17 vol.%. We conclude that the DEM model could not resolve elastic properties of Muderong Shale satisfactorily.

DISCUSSION

Elastic properties of shales have been of long-standing interest (e.g., Rundle and Schuler, 1981; Hornby et al., 1994; Sayers, 1994; Jakobsen et al., 2000; Dræge et al., 2006; Bayuk et al., 2007). Vasin et al. (2013) propose two models based on quantitative information about mineral composition, microstructure, and preferred orientations that could be used to describe experimentally measured elastic coefficients of Kimmeridge Shale (Hornby, 1998).

Here, we tested these two models with Muderong Shale. It contains 71.7 vol.% of phyllosilicates compared with 66.8 vol.% in the case of Kimmeridge Shale (Vasin et al. [2013], Table 1) but almost no feldspars or pyrite. Preferred orientations of phyllosilicates are different. In the Muderong Shale, they show higher degrees of preferred orientation (Table 1). Examination of the ODFs shows that higher texture strength of phyllosilicates in Muderong Shale is due to the lower volume fraction of randomly oriented grains; minimum (001) pole densities are 0.03–0.34 m.r.d., depending on the mineral, whereas for the Kimmeridge Shale they were 0.19–0.42 m.r.d. (Vasin et al., 2013). Maximum (001) pole density values for phyllosilicates in the Muderong Shale are also lower than in the Kimmeridge Shale; thus, distributions of pole densities on the main pole figures of phyllosilicates are broader. Illite-mica is derived from the diagenetic alteration process of biotite as indicated by iron content. The large crystals point to a detrital origin. Disordered illite-smectite, on the other hand, has weakest preferred orientation and small crystallites, which are likely authigenic, as documented by transmission electron microscopy (TEM) observations in other shales (e.g., Kanitpanyacharoen et al., 2011; Vasin et al., 2013).

Before discussing the modeling results, we should highlight some of the limitations. First, elastic properties of phyllosilicate clay minerals are poorly known due to the complexity of their structures. For

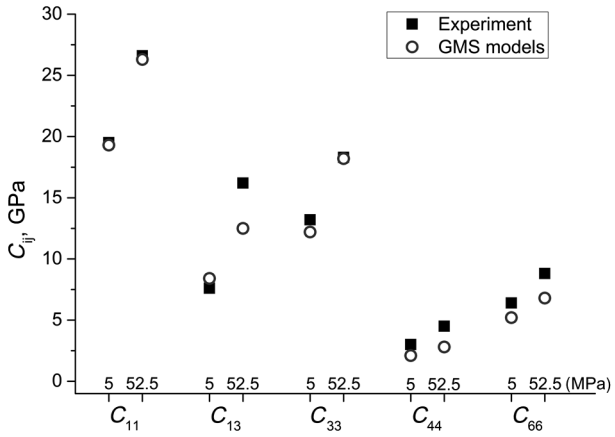

Figure 5. A comparison of C_{ij} of the GMS models no. 1 and 5 (Table 3) and ultrasonic velocity measurements at 5 and 52.5 MPa (Dewhurst and Siggins, 2006).

chlorite, we had to use elastic coefficients of quasihexagonal biotite measured by Aleksandrov and Ryzhova (1961). For other phyllosilicates, e.g., kaolinite and illite-smectite, there are only model elastic properties available. It is likely that elastic properties vary with details of chemical composition, ion exchange capacity, polytype, and water content (e.g., Suter et al., 2007; Mazo et al., 2008). The volume, shape, and distribution of organic content (kerogen) are other factors that can affect the elastic properties (e.g., Vernik and Nur, 1992). The Muderong Shale has a relatively low kerogen content (Figure 1), and thus this factor should not significantly influence elastic properties. In addition, we substitute actual shapes of grains and pores with fixed-axis ellipsoids, which may be an oversimplification (see the discussion in Vasin et al., 2013). Other irregular pore shapes (e.g., Loucks et al., 2009) have also not been included in our model.

Obviously complex distributions of pore shapes and sizes exist in shales. Quantification of every type of distribution and its use in the modeling procedures is currently impossible. Further complications arise if we consider the fact that, in principle, pores of different shapes could be related to different microstructural features of the material and consequently have different orientation distributions. Different elastic coefficients could also be attributed to different pores. Here, we substitute the real distribution with only two types of pores. Spherical pores stand for all high-aspect-ratio pores $\{1:1:z\}$ with the z-value being roughly higher than 0.5 (such pores influence bulk elastic properties of material almost in the same manner as spherical pores). Low-aspect-ratio pores (with certain fiber orientation distribution) describe the rest of the distribution of pores on shape. Based on these principles, we still have two open parameters to describe porosity, the *total porosity* that was estimated for Muderong Shale at ambient pressure only (Dewhurst and Siggins, 2006) and the ratio between volumes of spherical and low-aspect-ratio pores. The latter one, as documented by Vasin et al. (2013), could be close to 1:1. In principle, this ratio should reflect to a certain extent a real distribution of pores on shape. It is thus expected that for different shales with, e.g., different degrees of compaction, this ratio may be different. For example, in the study of Ruiz and Azizov (2011), the same two types of pores with aspect ratios $\{1:1:1\}$ and $\{1:1:0.01\}$ are used to describe elastic properties of a low-porosity Barnett Shale. However, in their models (featuring elastically isotropic mineral aggregates) the part of low-aspect-ratio pores in total porosity was less than 25%.

The volume fraction of pores with low aspect ratios greatly influences bulk elastic properties as shown by results of model nos. 2, 4, and 5 in Table 3. The C_{ij} values of model no. 2 calculated with porosity of 15 vol.% are higher than those of models nos. 4 and 5, which are modeled with porosities of 15.8 vol.% and 15.5 vol.%, respectively (including 0.1% empty pores). On the other hand, as noted by Le Ravalec and Guéguen (1996) for an isotropic medium and Vasin et al. (2013) for anisotropic Kimmeridge Shale, the addition of small amounts of spherical pores into a model almost linearly decreases all the bulk elastic coefficients. For example, adding an extra 0.5 vol.% of spherical water-filled pores into model no. 2 (Table 3) will decrease all elastic coefficient values by only ≈1%, and they will still be comparable with experimentally determined values. To compensate for this decrease (especially for elastic coefficients C_{33} and C_{44}), a very low amount (e.g., 0.05 vol.%) of low-aspect-ratio pores could be removed from the model. Thus, to a certain extent, total porosity and *ratio between volumes of spherical and low-aspect-ratio pores* in the model could be tuned without significant discrepancies between the model and measured elastic properties of the Muderong Shale.

When describing elastic properties of the Muderong Shale at lower pressure (≈5 MPa), we added only low-aspect-ratio pores into the high-pressure model. In reality, the distribution of pores on shape changes with the change of pressure. According to Walsh (1965), lower aspect ratio pores are the first to close as the pressure increases. Thus, in our model approximation, we assume that the volume fraction of spherical pores in the material remain the same at all pressures, and we decrease the ratio between volumes of spherical and low-aspect-ratio pores, increasing the total porosity. We do not change the aspect ratio of pores because it is reasonable that, as thinner pores close, others become thinner. Additional complications could arise from the fact that orientation distributions of pores could also be different at different pressures. The elasticity of still-opened pores could depend on pore pressure. Dependencies of elastic wave velocities (and, consequently, elastic coefficients) on pressure usually demonstrate a characteristic behavior described with combination of fast (exponential) and linear increase terms (e.g., Eberhart-Phillips et al., 1989; Pros et al., 1998; Ullemeyer et al., 2011). Attempts were made to explain this trend by two types of pores — soft and stiff — existing in the material (Shapiro, 2003; Pervukhina et al., 2010). With respect to pore closure with pressure, low-aspect-ratio pores could be considered as "soft" and spherical pores as "stiff" (Ruiz and Azizov, 2011).

Our calculated density of the crystalline part 2.751 g/cm^3 is significantly higher than the actual bulk density of the shale (2.33 g/cm^3) at atmospheric pressure. Partially this is due to the yet unaccounted porosity. Model no. 2 (Table 3) has a calculated density value of 2.488 g/cm^3, and model no. 5 (Table 3) of 2.479 g/cm^3, assuming the density value of 1.0 g/cm^3 for water-filled and zero for air-filled pores. It is possible that phyllosilicate densities that we consider could be over- or underestimated because they have been calculated based on "ideal" compositions, not including possible chemical and structural variations. For consistency, to calculate elastic wave velocities in all our models, we use the only available experimental density value of 2.33 g/cm^3. We note again that total porosity of models are to a certain extent "tunable," and this could be used to adjust model density to be closer to the experimentally determined value (at normal pressure), e.g., by adding small fractions of spherical pores. Results of GMS-based models nos. 2 and 5 (Table 3) and experimental elastic properties of Muderong Shale at ≈50 – 60 MPa and ≈5 MPa are shown in Figure 5.

Experimental C_{ij} values of Muderong Shale are derived from measured elastic wave velocities. In turn, model C_{ij} values could be used to calculate velocities. We will discuss them together to highlight differences and possible sources of errors. Velocities and elastic constants are related by means of the following equations (Dewhurst and Siggins, 2006):

$$V_{\mathrm{Pv}} = (C_{33}/\rho)^{1/2},$$
$$V_{\mathrm{Ph}} = (C_{11}/\rho)^{1/2},$$
$$V_{\mathrm{S1}} = (C_{44}/\rho)^{1/2},$$
$$V_{\mathrm{Sh}} = (C_{66}/\rho)^{1/2},$$

and

$$C_{13} = (-C_{44} + [4\rho^2 q V_{\mathrm{P45}}^4 - 2\rho q V_{\mathrm{P45}}^2 (C_{11} + C_{33} + 2C_{44}) + (C_{11} + C_{44})(C_{33} + C_{44})]$$

where V_{Pv} is the P-wave velocity along the axis of rotational symmetry (the bedding normal), V_{Ph} is the P-wave velocity parallel to the bedding, V_{S1} is the S-wave velocity normal to the bedding with polarization parallel to bedding, V_{Sh} is the S-wave velocity parallel to the bedding with polarization parallel to the bedding, qV_{P45} is the quasi-P-wave phase velocity 45° to bedding, and ρ is the bulk density.

Comparing the experimental results to those from the GMS model (Figure 5), it seems that the elastic moduli for P-waves traveling normal and parallel to the bedding (C_{33} and C_{11}, respectively) are well predicted at low and high pressure. The elastic coefficients associated with S-wave propagation (C_{44} and C_{66}) are less well predicted at low and high pressure, with larger deviations at the higher pressure level. In this case, the model always underestimates C_{44} and C_{66} when compared with the experiment, and though absolute difference in values is rather low — within 2 GPa — values of C_{44} and C_{66} are also low (less than 10 GPa). Finally, C_{13} (derived from the single quasi-P-wave velocity at 45° to the bedding) matches reasonably well at low pressure but poorly at high pressure. Errors of elastic constants reported in Dewhurst and Siggins (2006) are less than 1%, except for C_{13}, which was closer to 2%. Uncertainties in calculating C_{13} are a result of using a single off-axis raypath.

As a consequence of the differences in C_{ij}'s, differences in ultrasonic velocity profiles are observed (Figure 6). For the high pressure model no. 2 (Table 3), velocities of P-waves traveling normal and parallel to bedding are consistent with experimental measurements (Figure 6a). The underestimation of C_{44} and C_{66} in the GMS model no. 2 leads to the systematic underestimation of pure S-wave velocities (phase and group, Figure 6c). In addition, the result of the underestimation of C_{44} and especially C_{13} is that in GMS model no. 2 quasi-S-wave velocities, phase and group, in oblique directions are higher than in the bedding plane and normal to the bedding, but the reverse is true for the wave velocities recalculated from experimental elastic coefficients model no. 3 (Table 3). In the latter case, quasi-S-wave velocities in oblique directions are generally lower than in the bedding place and normal to the bedding (Figure 6b). Also, the model S-wave splitting distribution (for phase velocities only because for group velocities, there are directions in which more than two S-waves exist) has an additional minimum — zero splitting — in the direction about 43° to the bedding normal (Figure 6d), whereas S-wave splitting distribution derived from experimental elastic coefficients (no. 3) has an absolute maximum in the direction about 57° to the bedding normal.

It is interesting to quantify the observed decrease of elastic coefficients with the decrease of pressure. At low pressure (5 MPa), all experimental and model C_{ij} values are 1.3–1.5 times lower than at high pressure (52.5 MPa). The only exception is the experimental C_{13} value that is ≈2.1 times lower than at high pressure. In some ways, the large mismatch in C_{13} at high pressure is not surprising because the values calculated from experimental velocities are likely less accurate because they depend on a single off-axis P-wave measurement and an uncertain raypath. Using multiple raypath methods and inversion would provide more robust estimates (e.g., Nádri et al., 2011, 2012; Petružálek et al., 2013). A similar argument could be used for the discrepancies between the S-wave velocities in measurements and models. The largest variations are again at high pressure levels, although this is where there is the least uncertainty in picking S-wave arrivals experimentally. Dewhurst and Siggins (2006) suggest that the experimental error of S-wave velocities might be due to the stress-induced loss of interlayer water and the stiffening of the smectite structure. These effects can contribute to the underestimation of S-wave velocities especially at high stresses, and our models did not take them into account.

DEM model no. 7 (Table 3) provides a reasonable set of elastic coefficients, but only at very high total porosity of 27.2 vol.%, which is not supported by experiments. Vasin et al. (2013) note that even though for the Kimmeridge Shale this model provided good numerical results, it has two questionable characteristics. First, the mineral/water volume ratio at the start of DEM procedure could be selected within the 40/60–60/40 interval. This selection is fairly arbitrary because it is not constrained by any experimental data, but the selected ratio greatly influences the resulting elastic constants of the medium, e.g., C_{33} and C_{44}. Second, geometric mean averaging is used to average the elastic properties of constructed DEM units over ODFs and volume fractions. Even though mathematically the application of the geometric mean in elastic constants averaging is well justified, it does not have a clear relationship to the micromechanics of the sample, as do, e.g., the Voigt or Reuss models. Often, the geometric mean provides results that are close to the results of self-consistent or finite-element constructions. But in the case of very anisotropic phyllosilicate/water DEM units, results of these methods could differ substantially. Thus, we conclude that, at least

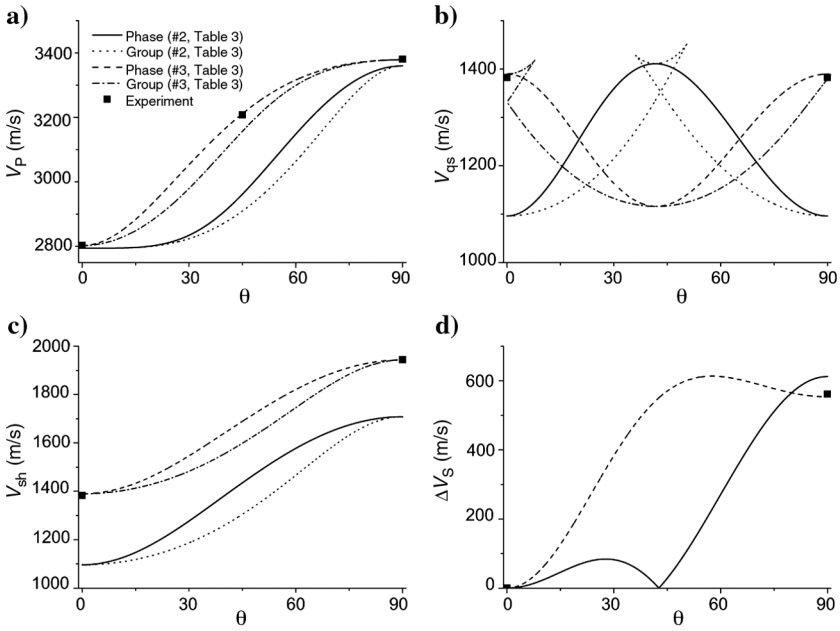

Figure 6. Velocities of (a) quasilongitudinal, (b) quasishear, and (c) shear elastic waves in Muderong Shale at 52.5 MPa (experiment and elastic constants estimation [Dewhurst and Siggins, 2006], no. 3 in Table 3) and shale model no. 2 (Table 3). S-wave splitting (phase velocities) is also shown in panel (d). The θ is the angle (in degrees) between the bedding plane normal and propagation direction (for phase velocities) or the group velocity vector direction (for group velocities).

in the case of the Muderong Shale, the DEM model does not provide a satisfactory solution.

CONCLUSIONS

Phyllosilicate minerals in Muderong Shale show high degrees of preferred orientation similar to previous studies on shales from different environments. These preferred orientation distributions serve as the basis for calculating elastic properties. By averaging this quantitative microstructural information with corresponding phase volumes, density, single crystal elastic stiffness, and aspect ratios in a self-consistent approach, a satisfactory agreement with experimental elastic properties, including velocities and anisotropy parameters, can be achieved. The approach appears to be robust and reliable to relate microstructural features to elastic responses of the Muderong Shale. Major uncertainties on the modeling side are single crystal elastic properties as well as quantitative assessments of pore distributions on orientations and shape. On the experimental side, multiple path methods of elastic wave velocity measurements may better constrain measured elastic properties.

ACKNOWLEDGMENTS

The authors would like to acknowledge support from National Science Foundation (NSF) (EAR-1343908) and Department of Energy (DOE) (DE-FG02-05ER15637) and access to the beamline 11-ID-C at the Advanced Photon Source of the Argonne National Laboratory. We also appreciate assistance from Y. Ren for the diffraction experiment; T. Teague for sample preparation; and useful comments from editors E. Slob, M. van der Baan, J. Shragge, and two anonymous reviewers.

REFERENCES

Aleksandrov, K. S., and T. V. Ryzhova, 1961, The elastic properties of rock-forming minerals, II: Layered silicates: Bulletin of the Academy of Sciences of the USSR, **12**, 1799–1804.

Antao, S. M., I. Hassan, J. Wang, P. L. Lee, and B. H. Toby, 2008, State-of-the-art high-resolution powder X-ray diffraction (HRPXRD) illustrated with Rietveld structure refinement of quartz, sodalite, tremolite, and meionite: Canadian Mineralogist, **46**, 1501–1509, doi: 10.3749/canmin.46.5.1501.

Aplin, A. C., and S. R. Larter, 2005, Fluid flow, pore pressure, wettability and leakage in mudstone cap rocks, *in* P. Boult, and J. Kaldi, eds., Evaluating fault and cap rock seals: Hedberg Series no. 2, AAPG, 1–12.

Aplin, A. C., I. F. Matenaar, D. K. McCarty, and B. A. van Der Pluijm, 2006, Influence of mechanical compaction and clay mineral diagenesis on the microfabric and pore-scale properties of deep-water Gulf of Mexico mudstones: Clays and Clay Minerals, **54**, 500–514, doi: 10.1346/CCMN.2006.0540411.

Arns, C. H., M. A. Knackstedt, W. Val Pinczewski, and E. J. Garboczi, 2002, Computation of linear elastic properties from microtomographic images: Methodology and agreement between theory and experiment: Geophysics, **67**, 1396–1405, doi: 10.1190/1.1512785.

Bayuk, I. O., M. Ammerman, and E. M. Chesnokov, 2007, Elastic moduli of anisotropic clay: Geophysics, **72**, no. 5, D107–D117, doi: 10.1190/1.2757624.

Bish, D. L., and R. B. Von Dreele, 1989, Rietveld refinement of non-hydrogen atomic positions in kaolinite: Clays and Clay Minerals, **37**, 289–296, doi: 10.1346/CCMN.1989.0370401.

Bossart, P., and M. Thury, 2007, Research in the Mont Terri Rock laboratory: Quo vadis?: Physics and Chemistry of the Earth, **32**, 19–31, doi: 10.1016/j.pce.2006.04.031.

Bruggeman, V. D., 1935, Berechnung verschiedener physikalischer Konstanten von heterogenen Substanzen. I. Dielektrizitätskonstanten und Leitfähigkeiten der Mischkörper aus isotropen Substanzen: Annalen der Physik, **416**, 636–664, doi: 10.1002/andp.19354160705.

Budiansky, B., 1965, On the elastic moduli of some heterogeneous materials: Journal of the Mechanics and Physics of Solids, **13**, 223–227, doi: 10.1016/0022-5096(65)90011-6.

Cockbain, A. E., and R. M. Hocking, 1989, Revised stratigraphic nomenclature in Western Australian Phanerozoic basins: Geological Survey of Western Australia.

Dellinger, J., and L. Vernick, 1994, Do traveltimes in pulse-transmission experiments yield group or phase velocities?: Geophysics, **59**, 1774–1779, doi: 10.1190/1.1443564.

Dewhurst, D. N., and A. L. Hennig, 2003, Geomechanical properties related to top seal leakage in the Carnarvon Basin, Northwest Shelf, Australia: Petroleum Geoscience, **9**, 255–263, doi: 10.1144/1354-079302-557.

Dewhurst, D. N., R. M. Jones, and M. D. Raven, 2002, Microstructural and petrophysical characterization of Muderong Shale: Application to top seal risking: Petroleum Geoscience, **8**, 371–383, doi: 10.1144/petgeo.8.4.371.

Dewhurst, D. N., and A. F. Siggins, 2006, Impact of fabric microcracks and stress field on shale anisotropy: Geophysical Journal International, **165**, 135–148, doi: 10.1111/j.1365-246X.2006.02834.x.

Dræge, A., M. Jakobsen, and T. A. Johansen, 2006, Rock physics modelling of shale diagenesis: Petroleum Geoscience, **12**, 49–57, doi: 10.1144/1354-079305-665.

Eberhart-Phillips, D., D.-H. Han, and M. D. Zoback, 1989, Empirical relationships among seismic velocity, effective pressure, porosity and clay content in sandstone: Geophysics, **54**, 82–89, doi: 10.1190/1.1442580.

Eshelby, J. D., 1957, The determination of the elastic field of an ellipsoidal inclusion, and related problems: Proceedings of the Royal Society of London, Series A: Mathematical, Physical and Engineering Sciences, **241**, 376–396, doi: 10.1098/rspa.1957.0133.

Fjær, E., R. M. Holt, P. Horsrud, A. M. Raaen, and R. Risnes, 2008, Petroleum related rock mechanics, 2nd ed.: Developments in Petroleum Science, vol. 33, Elsevier.

Gualtieri, A. F., 2000, Accuracy of XRPD QPA using the combined Rietveld-RIR method: Journal of Applied Crystallography, **33**, 267–278, doi: 10.1107/S002188989901643X.

Helbig, K., and M. Schoenberg, 1987, Anomalous polarization of elastic waves in transversely isotropic media: Journal of the Acoustical Society of America, **81**, 1235–1245, doi: 10.1121/1.394527.

Heyliger, P., H. Ledbetter, and S. Kim, 2003, Elastic constants of natural quartz: Journal of the Acoustical Society of America, **114**, 644–650, doi: 10.1121/1.1593063.

Hill, R., 1965, A self-consistent mechanics of composite materials: Journal of the Mechanics and Physics of Solids, **13**, 213–222, doi: 10.1016/0022-5096(65)90010-4.

Hornby, B. E., 1998, Experimental laboratory determination of the dynamic elastic properties of wet, drained shales: Journal of Geophysical Research: Solid Earth, **103**, 29945–29964, doi: 10.1029/97JB02380.

Hornby, B. E., L. M. Schwartz, and J. A. Hudson, 1994, Anisotropic effective-medium modeling of the elastic properties of shales: Geophysics, **59**, 1570–1583, doi: 10.1190/1.1443546.

Jakobsen, M., J. A. Hudson, T. A. Minshull, and S. C. Singh, 2000, Elastic properties of hydrate-bearing sediments using effective medium theory: Journal of Geophysical Research: Solid Earth, **105**, 561–577, doi: 10.1029/1999JB900190.

Johnston, D. H., 1987, Physical properties of shale at temperature and pressure: Geophysics, **52**, 1391–1401, doi: 10.1190/1.1442251.

Jones, L. E. A., and H. F. Wang, 1981, Ultrasonic velocities in Cretaceous shales from the Williston basin: Geophysics, **46**, 288–297, doi: 10.1190/1.1441199.

Joswig, W., H. Fuess, R. Rothbauer, Y. Takéuchi, and S. A. Mason, 1980, A neutron diffraction study of a one-layer triclinic chlorite (penninite): American Mineralogist, **65**, 349–352.

Kaarsberg, E. A., 1959, Introductory studies of natural and artificial argillaceous aggregates by sound propagation and x-ray diffraction methods: Journal of Geology, **67**, 447–472, doi: 10.1086/626597.

Kanitpanyacharoen, W., F. B. Kets, H.-R. Wenk, and R. Wirth, 2012, Mineral preferred orientation and microstructure in the Posidonia shale in relation to different degrees of thermal maturity: Clays and Clay Minerals, **60**, 315–329, doi: 10.1346/CCMN.2012.0600308.

Kanitpanyacharoen, W., H.-R. Wenk, F. Kets, C. Lehr, and R. Wirth, 2011, Texture and anisotropy analysis of Qusaiba shales: Geophysical Prospecting, **59**, 536–556, doi: 10.1111/j.1365-2478.2010.00942.x.

Keller, L. M., L. Holzer, P. Schuetz, and P. Gasser, 2013, Pore space relevant for gas permeability in Opalinus clay: Statistical analysis of homogeneity, percolation, and representative volume element: Journal of Geophysical Research: Solid Earth, **118**, 2799–2812, doi: 10.1002/jgrb.50228.

Keller, L. M., L. Holzer, R. Wepf, and P. Gasser, 2011, 3D geometry and topology of pore pathways in Opalinus clay: Implications for mass transport: Applied Clay Science, **52**, 85–95, doi: 10.1016/j.clay.2011.02.003.

Kennedy, M. J., D. R. Pevear, and R. J. Hill, 2002, Mineral surface control of organic carbon in black shale: Science, **295**, 657–660, doi: 10.1126/science.1066611.

Kröner, E., 1958, Berechnung der elastischen Konstanten des Vielkristalls aus den Konstanten des Einkristalls: Zeitschrift für Physik, **151**, 504–518, doi: 10.1007/BF01337948.

Kuila, U., and M. Prasad, 2013, Specific surface area and pore-size distribution in clays and shales: Geophysical Prospecting, **61**, 341–362, doi: 10.1111/1365-2478.12028.

Le Ravalec, M., and Y. Guéguen, 1996, High- and low-frequency elastic moduli for a saturated porous/cracked rock — Differential self-consistent and poroelastic theories: Geophysics, **61**, 1080–1094, doi: 10.1190/1.1444029.

Loucks, R. G., R. M. Reed, S. C. Ruppel, and U. Hammes, 2012, Spectrum of pore types and networks in mudrocks and a descriptive classification for matrix-related mudrock pores: AAPG Bulletin, **96**, 1071–1098, doi: 10.1306/08171111061.

Loucks, R. G., R. M. Reed, S. C. Ruppel, and D. M. Jarvie, 2009, Morphology, genesis, and distribution of nanometer-scale pores in siliceous mudstones of the Mississippian Barnett Shale: Journal of Sedimentary Research, **79**, 848–861, doi: 10.2110/jsr.2009.092.

Lutterotti, L., S. Matthies, H.-R. Wenk, A. S. Schultz, and J. W. Richardson, 1997, Combined texture and structure analysis of deformed limestone from time-of-flight neutron diffraction spectra: Journal of Applied Physics, **81**, 594–600, doi: 10.1063/1.364220.

Lutterotti, L., M. Voltolini, H.-R. Wenk, K. Bandyopadhyay, and T. Vanorio, 2010, Texture analysis of turbostratically disordered Ca-montmorillonite: American Mineralogist, **95**, 98–103, doi: 10.2138/am.2010.3238.

Mallants, D., J. Marivoet, and X. Sillen, 2001, Performance assessment of the disposal of vitrified high-level waste in a clay layer: Journal of Nuclear Materials, **298**, 125–135, doi: 10.1016/S0022-3115(01)00577-3.

Matthies, S., 2010, On the combination of self-consistent and geometric mean elements for the calculation of the elastic properties of textured multi-phase samples: Solid State Phenomena, **160**, 87–93, doi: 10.4028/www.scientific.net/SSP.160.87.

Matthies, S., 2012, GEO-MIX-SELF calculations of the elastic properties of a textured graphite sample at different hydrostatic pressures: Journal of Applied Crystallography, **45**, 1–16, doi: 10.1107/S002188981104338X.

Matthies, S., and M. Humbert, 1995, On the principle of a geometric mean of even-rank symmetric tensors for textured polycrystals: Journal of Applied Crystallography, **28**, 254–266, doi: 10.1107/S0021889894009623.

Matthies, S., and G. W. Vinel, 1982, On the reproduction of the orientation distribution function of textured samples from reduced pole figures using the conception of a conditional ghost correction: Physica Status Solidi b, **112**, K111–K114, doi: 10.1002/pssb.2221120254.

Matthies, S., and H.-R. Wenk, 2009, Transformations for monoclinic crystal symmetry in texture analysis: Journal of Applied Crystallography, **42**, 564–571, doi: 10.1107/S0021889809018172.

Matthies, S., H.-R. Wenk, and G. W. Vinel, 1988, Some basic concepts of texture analysis and comparison of three methods to calculate orientation distributions from pole figures: Journal of Applied Crystallography, **21**, 285–304, doi: 10.1107/S0021889888000275.

Mazo, M. A., L. I. Manevitch, E. B. Gusarova, M. Y. Shamaev, A. A. Berlin, N. K. Balabaev, and G. C. Rutledge, 2008, Molecular dynamics simulation of thermomechanical properties of montmorillonite crystal. II. Hydrate montmorillonite cristal: Journal of Physical Chemistry. C, **112**, 17056–17062, doi: 10.1021/jp711188u.

Militzer, B., H.-R. Wenk, S. Stackhouse, and L. Stixrude, 2011, First-principles calculation of the elastic moduli of sheet silicates and their application to shale anisotropy: American Mineralogist, **96**, 125–137, doi: 10.2138/am.2011.3558.

Morris, P. R., 1970, Elastic constants of polycrystals: International Journal of Engineering Science, **8**, 49–61, doi: 10.1016/0020-7225(70)90014-5.

Moyano, B., K. T. Spikes, T. A. Johansen, and N. H. Mondol, 2012, Modeling compaction effects on the elastic properties of clay-water composites: Geophysics, **77**, no. 5, D171–D183, doi: 10.1190/geo2011-0426.1.

Nadri, D., A. Bóna, M. Brajanovski, and T. Lokajíček, 2011, Estimation of stress-dependent anisotropy from P-wave measurements on a spherical sample: Geophysics, **76**, no. 3, WA91–WA100, doi: 10.1190/1.3552703.

Nadri, D., J. Sarout, A. Bóna, and D. Dewhurst, 2012, Estimation of anisotropy parameters of transversely isotropic shales with a tilted symmetry axis: Geophysical Journal International, **190**, 1197–1203, doi: 10.1111/j.1365-246X.2012.05545.x.

Nur, A., and G. Simmons, 1969, The effect of saturation on velocity in low porosity rocks: Earth and Planetary Science Letters, **7**, 183–193, doi: 10.1016/0012-821X(69)90035-1.

Ortega, A. J., F.-J. Ulm, and Y. Abousleiman, 2007, The effect of nanogranular nature of shale on their poroelastic behavior: Acta Geotechnica, **2**, 155–182, doi: 10.1007/s11440-007-0038-8.

Pervukhina, M., B. Gurevich, D. N. Dewhurst, and A. F. Siggins, 2010, Applicability of velocity-stress relationships based on the dual porosity concept to isotropic porous rocks: Geophysical Journal International, **181**, 1473–1479, doi: 10.1111/j.1365-246X.2010.04535.x.

Petružálek, M., J. Vilhelm, V. Rudajev, T. Lokajíček, and T. Svitek, 2013, Determination of the anisotropy of elastic waves monitored by a sparse sensor network: International Journal of Rock Mechanics and Mining Sciences, **60**, 208–216, doi: 10.1016/j.ijrmms.2012.12.020.

Pham, N. H., J. M. Carcione, H. B. Helle, and B. Ursin, 2002, Wave velocities and attenuation of shaley sandstones as a function of pore pressure and partial saturation: Geophysical Prospecting, **50**, 615–627, doi: 10.1046/j.1365-2478.2002.00343.x.

Plançon, A., S. I. Tsipurski, and V. A. Drits, 1985, Calculation of intensity distribution in the case of oblique texture electron diffraction: Journal of Applied Crystallography, **18**, 191–196, doi: 10.1107/S0021889885010147.

Pros, Z., T. Lokajíček, and K. Klíma, 1998, Laboratory approach to study of elastic anisotropy on rock samples: Pure and Applied Geophysics, **151**, 619–629, doi: 10.1007/s000240050133.

Rietveld, H. M., 1969, A profile refinement method for nuclear and magnetic structures: Journal of Applied Crystallography, **2**, 65–71, doi: 10.1107/S0021889869006558.

Ruiz, F., and I. Azizov, 2011, Tight shale elastic properties using the soft-porosity and single aspect ratio models: 81st Annual International Meeting, SEG, Expanded Abstracts, 2241–2245.

Rundle, J. B., and K. W. Schuler, 1981, A composite model for the anisotropic elastic moduli of lean oil shale: Geophysics, **46**, 163–171, doi: 10.1190/1.1441186.

Sarout, J., L. Esteban, C. Delle Piane, B. Maney, and D. N. Dewhurst, 2014, Elastic anisotropy of Opalinus Clay under variable saturation and triaxial stress: Geophysical Journal International, **198**, 1662–1682, doi: 10.1093/gji/ggu231.

Sayers, C. M., 1994, The elastic anisotropy of shales: Journal of Geophysical Research: Solid Earth, **99**, 767–774, doi: 10.1029/93JB02579.

Sayers, C. M., 2008, The effect of low aspect ratio pores on the seismic anisotropy of shales: 78th Annual International Meeting, SEG, Expanded Abstracts, 2750–2754.

Shapiro, S. A., 2003, Elastic piezosensitivity of porous and fractured rocks: Geophysics, **68**, 482–486, doi: 10.1190/1.1567215.

Suter, J. L., P. V. Coveney, H. C. Greenwell, and M.-A. Thyveetil, 2007, Large-scale molecular dynamics study of montmorillonite clay: Emergence of undulatory fluctuations and determination of material properties: Journal of Physical Chemistry C, **111**, 8248–8259, doi: 10.1021/jp070294b.

Tao, Z., and A. Clarens, 2013, Estimating the carbon sequestration capacity of shale formations using methane production rates: Environmental Science and Technology, **47**, 11318–11325, doi: 10.1021/es401221j.

Tissot, B. P., and D. H. Welte, 1984, Petroleum formation and occurrence: SpringerVerlag.

Tsvankin, I., 2001, Seismic signatures and analysis of reflection data in anisotropic media: Elsevier Science.

Ufer, K., G. Roth, R. Kleeberg, H. Stanjek, R. Dohrmann, and J. Bergmann, 2004, Description of X-ray powder pattern of turbostratically disordered layer structures with a Rietveld compatible approach: Zeitschrift für Kristallographie, **219**, 519–527.

Ullemeyer, K., D. I. Nikolayev, N. I. Christensen, and J. H. Behrmann, 2011, Evaluation of intrinsic velocity-pressure trends from low-pressure P-wave velocity measurements in rocks containing microcracks: Geophysical Journal International, **185**, 1312–1320, doi: 10.1111/j.1365-246X.2011.05008.x.

Vasin, R., H.-R. Wenk, W. Kanitpanyacharoen, S. Matthies, and R. Wirth, 2013, Elastic anisotropy modeling of Kimmeridge shale: Journal of Geophysical Research: Solid Earth, **118**, 3931–3956, doi: 10.1002/jgrb.50259.

Vernik, L., and A. Nur, 1992, Ultrasonic velocity and anisotropy of hydrocarbon source rocks: Geophysics, **57**, 727–735, doi: 10.1190/1.1443286.

Voltolini, M., H.-R. Wenk, N. H. Mondol, K. Bjørlykke, and J. Jahren, 2009, Anisotropy of experimentally compressed kaolinite-illite-quartz mixtures: Geophysics, **74**, no. 1, D13–D23, doi: 10.1190/1.3002557.

Walsh, J. B., 1965, The effect of cracks on the compressibility of rocks: Journal of Geophysical Research, **70**, 381–389, doi: 10.1029/JZ070i002p00381.

Wang, Z., 2002, Seismic anisotropy in sedimentary rocks, Part 2: Laboratory data: Geophysics, **67**, 1423–1440, doi: 10.1190/1.1512743.

Wenk, H.-R., W. Kanitpanyacharoen, and M. Voltolini, 2010, Preferred orientation of phyllosilicates: Comparison of fault gouge, shale and schist: Journal of Structural Geology, **32**, 478–489, doi: 10.1016/j.jsg.2010.02.003.

Wenk, H.-R., L. Lutterotti, P. Kaercher, W. Kanitpanyacharoen, L. Miyagi, and R. N. Vasin, 2014, Rietveld texture analysis from synchrotron diffraction images. II. Complex multiphase materials and diamond anvil cell experiments: Powder Diffraction, **29**, 220–232, doi: 10.1017/S0885715614000360.

Wenk, H.-R., S. Matthies, J. Donovan, and D. Chateigner, 1998, BEARTEX: A Windows-based program system for quantitative texture analysis: Journal of Applied Crystallography, **31**, 262–269, doi: 10.1107/S002188989700811X.

Wenk, H.-R., M. Voltolini, H. Kern, T. Popp, and M. Mazurek, 2008, Anisotropy in shale from Mont Terri: The Leading Edge, **27**, 742–748, doi: 10.1190/1.2944159.

Xu, T., J. A. Apps, and K. Pruess, 2005, Mineral sequestration of carbon dioxide in a sandstone-shale system: Chemical Geology, **217**, 295–318, doi: 10.1016/j.chemgeo.2004.12.015.